

Cite this: *J. Mater. Chem. A*, 2023, **11**, 17581

Role of the energy offset in the charge photogeneration and voltage loss of nonfullerene acceptor-based organic solar cells†

Yasunari Tamai,¹ ^{ab} Rei Shirouchi,^a Toshiharu Saito,^a Kazuki Kohzuki^a and Shin-ichiro Natsuda^a

The trade-off between short-circuit current density (J_{SC}) and open-circuit voltage (V_{OC}) has been one of the largest challenges in improving the power conversion efficiencies (PCEs) of organic solar cells (OSCs). Although the energy offset between the excited and charge transfer (CT) states should remain minimal to achieve a high V_{OC} , a very small energy offset typically leads to degradation of J_{SC} , even when novel nonfullerene acceptors (NFAs), such as Y6, are used. Therefore, understanding the limit to what extent the energy offset can be minimized and the physics underlying the trade-off relationship is important to optimize the design of new materials and further improve the PCEs. This study provides a threshold energy that can ensure high charge photogeneration quantum efficiencies for Y-series NFA-based OSCs and discusses the role of the energy offset in device performances. We found that an insufficient energy offset led to not only slow hole transfer at the donor:acceptor interfaces, but also inefficient long-range spatial dissociation of the CT states and degradation of the fill factor (FF). This study also discusses the interplay of the energy levels of the two NFAs that constitute ternary blend OSCs. We found that, by introducing a low-efficiency NFA into a high-efficiency donor:acceptor blend, the voltage loss can be reduced while maintaining a high charge photogeneration quantum efficiency. Our findings highlight the importance of overcoming the trade-off between FF and V_{OC} for further improving the PCE.

Received 31st March 2023
Accepted 19th June 2023

DOI: 10.1039/d3ta01928d

rsc.li/materials-a

^aDepartment of Polymer Chemistry, Graduate School of Engineering, Kyoto University, Katsura, Nishikyo, Kyoto 615-8510, Japan. E-mail: tamai@photo.polym.kyoto-u.ac.jp
^bJapan Science and Technology Agency (JST), PRESTO, 4-1-8 Honcho, Kawaguchi, Saitama 332-0012, Japan

† Electronic supplementary information (ESI) available. See DOI: <https://doi.org/10.1039/d3ta01928d>



Yasunari Tamai received his PhD degree from Kyoto University in 2013 in the excited-state dynamics in nanostructured polymer systems. He joined the Optoelectronics group at the University of Cambridge as a postdoctoral fellow under the supervision of Prof. Sir Richard Friend, where his research focused on the ultrafast charge separation at organic semiconductor heterojunctions. Since

2016, he has been an Assistant Professor at Kyoto University. From 2018 to 2022, he was also a JST PRESTO researcher. His current research interests include exciton and charge dynamics in organic semiconductors, particularly conjugated polymers.

Introduction

The power conversion efficiencies (PCEs) of organic solar cells (OSCs) have rapidly improved in recent years and now exceed 19%.¹⁻⁷ Nevertheless, a large voltage loss ΔV , which is defined as the difference between the optical bandgap E_g and open-circuit voltage V_{OC} ($\Delta V = E_g/q - V_{OC}$, where q is the elementary charge), is a significant disadvantage of OSCs, restricting further improvement in the PCEs of OSCs.^{8,9} Although ΔV has continuously decreased in the past decade, state-of-the-art OSCs still exhibit ΔV s of ~ 0.5 V or more, which remains considerably larger than those of their inorganic and perovskite counterparts, where ΔV of less than 0.4 V can be achieved.¹⁰

Large voltage losses in OSCs primarily originate from the following two sources. The first source is the voltage loss incurred during the charge generation process as OSCs require donor:acceptor (D:A) heterointerfaces to split excitons into holes on the donors and electrons on the acceptors. The voltage loss associated with the charge generation process had been greater than 0.3 V because a large offset between the E_g and the charge transfer (CT) state energy E_{CT} of larger than 0.3 eV had been presumed to be required for efficient charge separation.^{8,11-14} In contrast, recent studies have shown that efficient charge separation with an energy offset of less than 0.3 eV can be achieved for various nonfullerene acceptor (NFA)-



based devices. We have revealed that a representative high-efficiency NFA-based OSC consisting of PBDB-T-2F (also referred to as PM6) and Y6 as an electron donor and acceptor, respectively, exhibits a near-unity and temperature-independent charge separation efficiency despite a small energy offset of ~ 0.12 eV.¹⁵ However, to what extent the energy offset can be minimized, while maintaining a high charge photogeneration quantum efficiency is unclear. Within the Marcus description for charge transfer,^{8,14,16} reduction of energy offset is inevitably disadvantageous for efficient charge separation.^{17–19} In fact, an OSC consisting of PBDB-T-2F paired with Y5 exhibited a poor photovoltaic external quantum efficiency (EQE_{PV}) of 36.1%, whereas ΔV of this device was ~ 80 mV smaller than that of the PBDB-T-2F:Y6 device owing to the smaller energy offset of the former.²⁰

The other source for the large ΔV s in OSCs is because of the voltage loss incurred during the charge recombination process. In the Shockley–Queisser (SQ) framework,²¹ nonradiative charge recombination leads to a non-ideal extra voltage loss ΔV_{nr} .^{9,17,20,22–26} Conventional fullerene-based OSCs typically exhibit ΔV_{nr} s of approximately 0.4 V,²⁵ which are substantially larger than those of their inorganic and perovskite counterparts. The origin of the large ΔV_{nr} can be rationalized by the extremely low photoluminescence quantum yields (PLQYs) of the CT states. When a free carrier encounters an opposite charge at the D:A interface, a CT state is regenerated at the interface followed by deactivation to the ground state. As CT states predominantly decay nonradiatively due to their significantly small oscillator strengths, charge recombination in fullerene-based OSCs leads to a large ΔV_{nr} s. This is also valid for NFA-based OSCs. For instance, the PBDB-T-2F:Y6 device exhibits a relatively large ΔV_{nr} of ~ 0.25 V.²⁰ Recent studies have highlighted the importance of reducing the energy offset in minimizing not only the voltage loss incurred during charge generation, but also the ΔV_{nr} .^{17,20,27,28} We have demonstrated that the ΔV_{nr} s of OSCs continuously decreased with a decrease in energy offset, and the abovementioned PBDB-T-2F:Y5 device exhibited a small ΔV_{nr} of 0.145 V while the PCE of this device was poor due to the low EQE_{PV}.^{17,20}

On the other hand, some recent reports have claimed that self-ionization of excitons without a heterojunction occurs in Y6 pristine films,^{29,30} and hence, donor polymers, such as PBDB-T-2F, only serve as hole transport materials to suppress the bimolecular charge recombination. If this is true and is an intrinsic property of the Y-series NFAs, the low EQE_{PV} of the abovementioned PBDB-T-2F:Y5 device may stem from other processes than charge separation. Therefore, again, it is crucial to unveil whether a D:A interface with a certain amount of energy offset is necessary for efficient charge separation and to what extent the energy offset can be minimized.

The ternary blend concept has been widely applied to OSCs to enhance the PCEs. Indeed, many state-of-the-art OSCs are ternary blend systems consisting of a common donor polymer and two NFAs (and *vice versa*).^{1–6} In ternary blend systems, upon changing the blend ratio of the two NFAs, V_{OC} continuously varies between V_{OC} s of the corresponding binary reference systems.^{31,32} In addition, several studies have shown that when

the two NFAs form co-crystals, the ionization energies (IEs) of the co-crystals can be continuously tuned between the IEs of the two NFAs, enabling precise control of the energy offset.³³ However, the role of the energy offsets of corresponding binary reference systems in the charge photogeneration and voltage loss has not been fully elucidated.

Herein, we studied the relationship between the energy offset and EQE_{PV} of NFA-based OSCs to discuss to what extent the energy offset can be minimized. We used PBDB-T-based donor polymers and Y-series NFAs with different highest occupied molecular orbital (HOMO) energies (Fig. 1) to ensure similar photon absorption efficiencies and E_g s with minimal difference in their chemical structures. This allowed us to focus on the impacts of energy offsets on the charge photogeneration and voltage losses. We prepared OSCs using 24 D:A combinations and examined the corresponding EQE_{PV}s and voltage losses. The EQE_{PV} sharply decreased when the voltage loss was less than 0.52 V. We found that an insufficient energy offset led to slow charge transfer at the D:A interfaces, as has been expected by Marcus theory. Surprisingly, the insufficient energy offset also resulted in poor long-range spatial dissociation of the CT states. This is contrary to the expectations derived from recent studies,³⁴ wherein the band bending near the D:A interface driven by the large quadrupole moments of NFAs was supposed to accelerate long-range charge dissociation once the CT states were formed, resulting in barrier-less efficient charge dissociation. Degradation of the fill factor (FF) with a decrease in the energy offset was also observed because of the inefficient charge dissociation. We also discuss the interplay of the energy levels of the two NFAs that constitute ternary blend OSCs. We found that combining two NFAs enables us to reduce the voltage loss overcoming the abovementioned threshold, while maintaining a high charge photogeneration quantum efficiency.

Results and discussion

Materials and ionization energies

We used three PBDB-T-based donors paired with eight Y-series acceptors (the chemical structure of the materials employed in this study can be found in Fig. 1), resulting in 24 combinations of D:A blends. We stress that the E_g s and absorption properties are similar among all the devices (steady-state absorption spectra are provided in Fig. S1, ESI†), allowing us to focus on the role of energy offset in the charge photogeneration and voltage loss. In contrast, the HOMO energy difference between the donor and acceptor can be substantially tuned with minimal differences in the chemical structure and associated changes in physical properties.

The HOMO energies (or IEs) of organic semiconductors are usually evaluated by photoelectron spectroscopic techniques, such as ultraviolet photoelectron spectroscopy (UPS) and photoelectron yield spectroscopy in air (PYSA), or by electrochemical techniques, such as cyclic voltammetry (CV). Recent studies have pointed out that the HOMO energy differences between the donor and NFA determined by the photoelectron spectroscopies were significantly larger than those determined



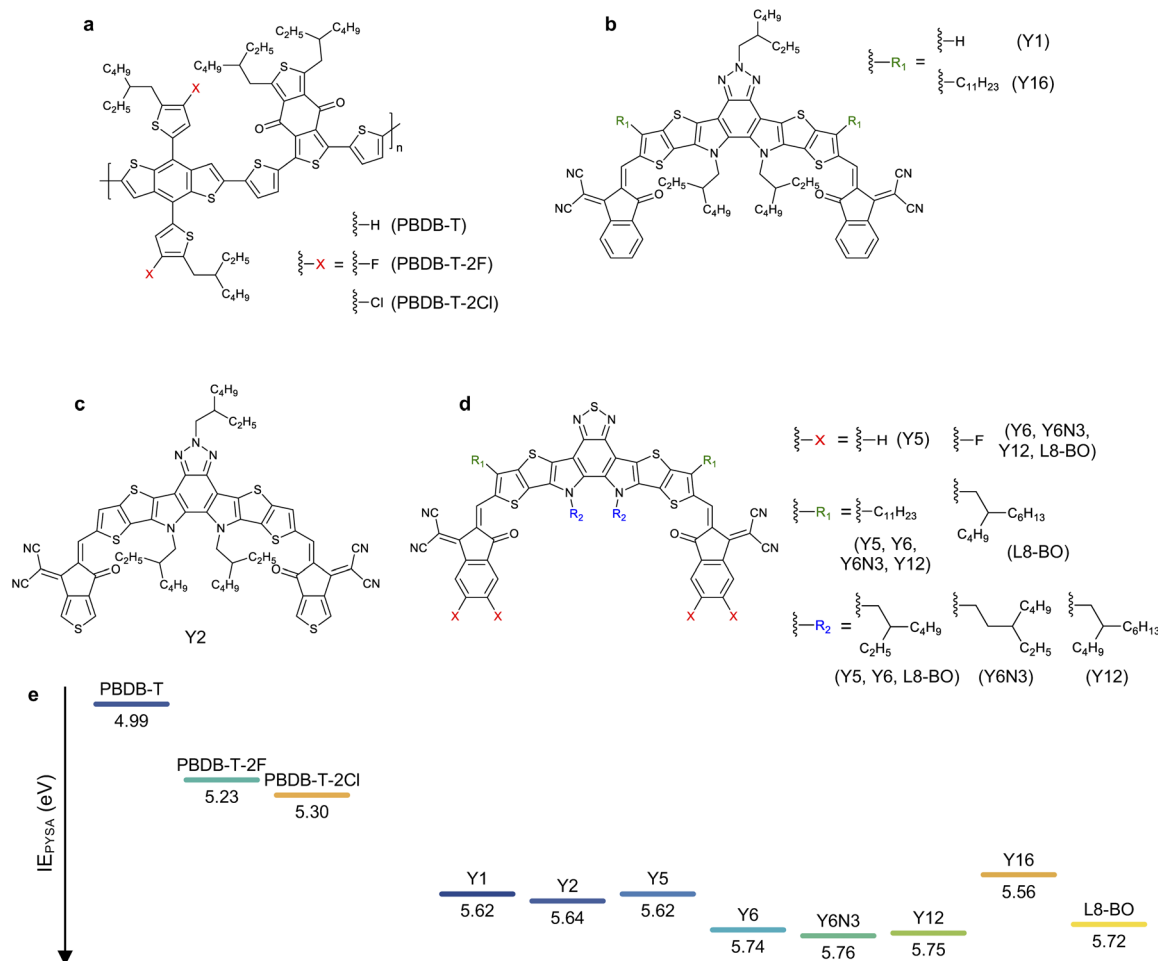


Fig. 1 Chemical structures of (a) donor and (b–d) acceptor materials employed in this study. PBDB-T-2F and PBDB-T-2Cl are also referred to as PM6 and PM7, respectively. (e) Ionization energies (IEs) of pristine donor and acceptor films determined by photoelectron yield spectroscopy in air (PYSA).

by CV.^{34–36} For instance, the HOMO energy difference between PBDB-T-2F and Y6 determined using CV was only ~ 0.1 eV,³⁵ whereas the IE differences of the same blend determined by UPS and PYSA were >0.5 eV.^{34,36} The origin of the large discrepancy between these was likely due to differences in sample morphology. Photoelectron spectroscopies probe the IEs of solid states (especially, near the surface). In contrast, materials used for CV measurements are more disordered than those used for photoelectron spectroscopies even when film samples are applied to CV measurements because the film is swollen by solvents or sometimes dissolves into solvents during measurements. This leads to large variations in the contributions caused by charge–permanent multipole (mainly quadrupole) interactions to the observed HOMO (IE),^{34,37} resulting in a large discrepancy in the measured values. Therefore, photoelectron spectroscopies are considered more reliable for determining the IEs of the “pure” donor and acceptor materials in the solid state; hence, this study determined the IE differences between the donor and acceptor materials in their pristine film state using PYSA ($\Delta\text{IE}_{\text{PYSA}}$). In contrast, it should be emphasized that the actual D:A interfaces in bulk heterojunction blends are

more disordered than pristine films. Therefore, the actual HOMO differences at the D:A interface likely differ from those determined for pristine films using photoelectron spectroscopies because the charge–permanent multipole interactions are supposedly weaker in the interfacial D:A mixed region. In fact, time-resolved spectroscopic techniques have shown that the energy offset between E_g and E_{CT} of the PBDB-T-2F:Y6 blend is only ~ 0.12 eV.¹⁵ This value is considerably smaller than the abovementioned IE difference determined using photoelectron spectroscopies, but similar to the value determined by CV measurements. Therefore, $\Delta\text{IE}_{\text{PYSA}}$ should be significantly larger than the actual HOMO energy difference at the D:A interface. Nevertheless, $\Delta\text{IE}_{\text{PYSA}}$ remains an effective quantitative measure of the energy offset. Fig. 1e shows the IEs of materials employed in this study determined by PYSA (experimental data can be found in Fig. S2, ESI†). These values are consistent with those reported previously with minor variations (see Fig. S3† for more details).³⁶ Note that the lowest unoccupied molecular orbital (LUMO) energies were estimated using IEs and excited state energies (Fig. S4, ESI†); thereby, these values only serve as a rough estimate for relative comparison. The



LUMO energy differences between the donor and acceptor materials were sufficiently large. However, because efficient energy transfer from the donor to the acceptor occurs, the LUMO energy difference was not related to device performances (*vide infra*).

Trade-off between charge generation and voltage loss

Fig. 2a and b show the current density–voltage (J – V) characteristics and EQE_{PV} spectra of four representative solar cell devices employed in this study (the experimental results and photovoltaic device parameters for all devices can be found in Fig. S5, S6 and Tables S4–S6, ESI[†]). We found a clear trade-off relationship between short-circuit current density (J_{SC}) and V_{OC} ; V_{OC} increased with a decrease in J_{SC} . EQE_{PV} also decreased with an increase in V_{OC} . These results suggest that the charge separation efficiency decreases with a decrease in the energy offset (*i.e.*, a decrease in ΔE_{PYSA}), as was observed for the conventional fullerene-based OSCs.^{13,38} Interestingly, the EQE_{PV} spectra followed well with the absorption spectra, indicating that the internal quantum efficiencies (IQEs) of these devices were less sensitive to the excitation wavelength despite large LUMO energy differences between the donor and acceptor. This is also confirmed using Fig. 2c, wherein the maximum EQE_{PV} in the near-IR region (>650 nm), which corresponds to the acceptor absorption region, is plotted against the maximum EQE_{PV} over the entire wavelength region (most devices showed the maximum EQE_{PV} in the visible region). Owing to the large spectral overlap between donor fluorescence and acceptor absorption, energy transfer from the donor to the acceptor is

likely to outcompete the electron transfer (Fig. S7, ESI[†])³⁹ This leads to predominant acceptor exciton formation regardless of the excitation wavelength, rendering EQE_{PV} insensitive to the excitation wavelength. Therefore, the maximum EQE_{PV} over the entire wavelength region is plotted against ΔV . Using the maximum EQE_{PV} value allows us to minimize the influence of imperfect photon absorption. As shown in Fig. 2d, EQE_{PV} drops sharply when ΔV is less than 0.52 V. The maximum EQE_{PV} is also plotted against the IE difference ΔE_{PYSA} (Fig. S8, ESI[†]), where we found that the threshold value of ΔE_{PYSA} that ensured efficient charge photogeneration was ~ 0.42 eV. We underline that the ΔE_{PYSA} used here, which was determined by the PYSA measurements for the pristine thin films, is considerably larger than the energy offset between E_g and E_{CT} owing to the contribution caused by charge–permanent multipole (mainly quadrupole) interactions, as mentioned above.

A similar trend was also observed for fullerene-based OSCs. However, the threshold value obtained in this study is lower than that observed for fullerene-based OSCs (see Fig. S10, ESI[†] for more details),^{13,38} indicating that Y-series NFAs can achieve an efficient charge photogeneration with a lower threshold voltage loss.

To obtain deeper insights, V_{OC} was divided into two parts, as follows:

$$V_{OC} = V_{OC}^{rad} - \Delta V_{nr} \quad (1)$$

where V_{OC}^{rad} is the radiative limit of V_{OC} , wherein charge recombination is always accompanied by photon emission (*i.e.*, the maximum achievable V_{OC} when the QY of radiative charge

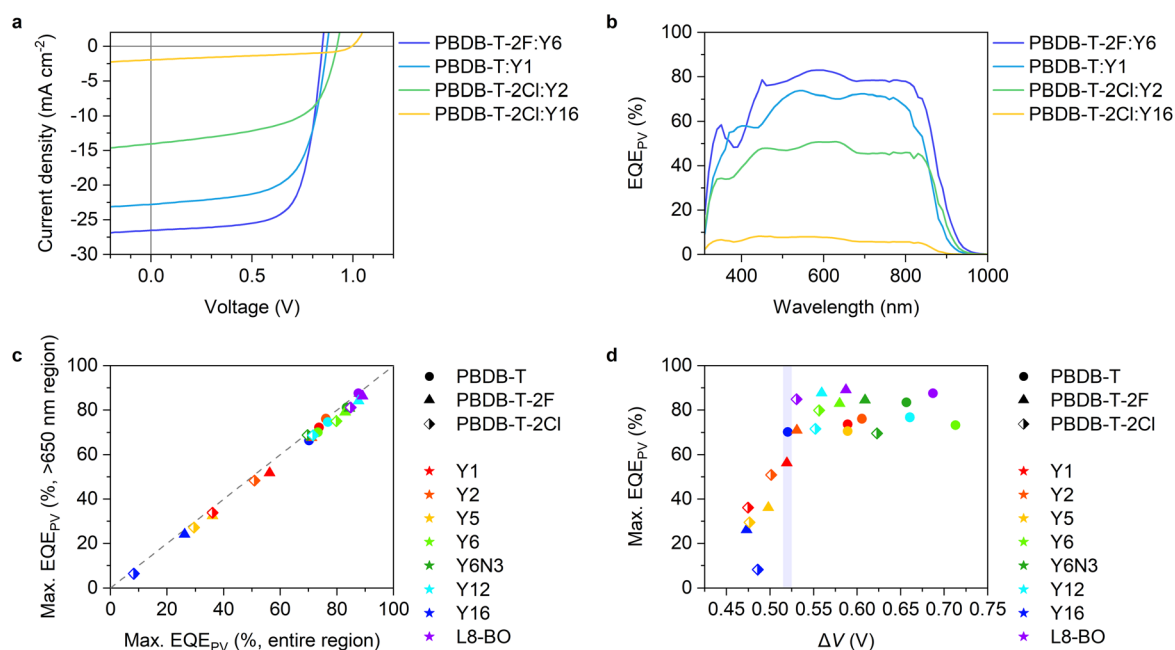


Fig. 2 (a) J – V characteristics and (b) EQE_{PV} spectra of the four representative devices. (c) Maximum EQE_{PV}s in the >650 nm region plotted against those over the entire wavelength region. (d) Maximum EQE_{PV} over the entire wavelength region plotted against ΔV ($= E_g/q - V_{OC}$). E_g was determined from the EQE_{PV} spectra using the method proposed earlier,²⁴ wherein the first derivative of the EQE_{PV} spectrum is assumed to be a probability distribution function of the photovoltaic bandgap energy, and the mean value of the distribution is used for E_g . The shape and color of the legends in (c) and (d) identify donors and acceptors, respectively.



recombination is unity). Tables S7 and S8† summarize V_{OC}^{rad} and ΔV_{nr} for all devices (see the ESI† for the details of the determination procedure). As the CT absorption was buried under the smeared-out absorption edge of acceptors for all devices owing to the small energy offset, V_{OC}^{rad} was largely determined by E_g , and hence, showed a narrow distribution of 1.100 ± 0.022 V. In contrast, ΔV_{nr} exhibited a significant variation ranging from 0.139 to 0.363 V. In other words, the variation of ΔV was mostly governed by that of ΔV_{nr} , as shown in Fig. S12.† As mentioned above, ΔV_{nr} significantly depends on the energy offset, indicating that ΔV_{nr} can be an alternative quantitative measure for the energy offset.²⁰ Therefore, as shown in Fig. 3a, the maximum EQE_{PV} values were also plotted against ΔV_{nr} . EQE_{PV} again showed a clear threshold at approximately 0.2 V; EQE_{PV} dropped sharply in the region where ΔV_{nr} was less than 0.2 V. This result is consistent with the fact that few OSCs reported to date exhibited high EQE_{PV} with ΔV_{nr} less than 0.2 V.⁹ Briefly, by plotting EQE_{PV} against the three different criteria (ΔV , ΔIE_{PYSAs} , and ΔV_{nr}), we observed a clear threshold above which efficient charge photogeneration could be ensured in any of the three criteria, indicating that a D:A interface with a certain amount of energy offset is required for efficient charge photogeneration, contrary to what some reports have claimed.^{29,30} Note that the V_{OC} and voltage losses are also affected by the morphology of the active layer. However, differences in morphology cannot explain the existence of the threshold energy observed in this study as morphology is independent of the energy offset.

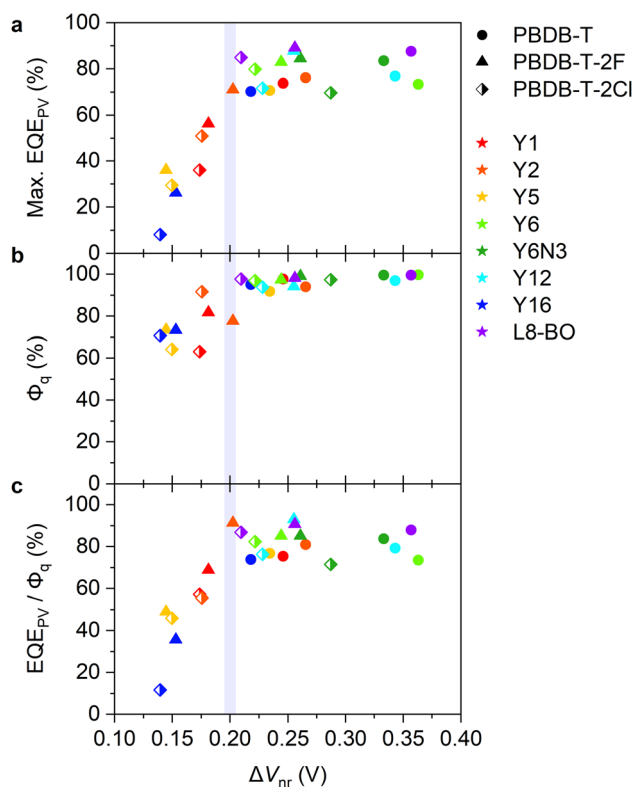


Fig. 3 (a) Maximum EQE_{PV}, (b) PL quenching yield Φ_q , and (c) EQE_{PV}/ Φ_q plotted against ΔV_{nr} .

Ideally, it is the most straightforward to discuss the relationship between EQE_{PV} and the energy offset between E_g and E_{CT} ; however, accurately determining the E_{CT} of some blends is challenging.⁸ For instance, E_{CT} can be determined by time-resolved PL measurements if the CT emission can be distinguished from the corresponding prompt emission.¹⁵ However, this requires a near-unity exciton dissociation and reasonable CT emission intensity. Hence, CT emission is buried under the corresponding prompt emission when any of these are not satisfied, making it impossible to determine E_{CT} from emission measurements. Therefore, we will use ΔV_{nr} as an alternative quantitative measure for the energy offset in the following sections. Plots using ΔIE_{PYSAs} can be found in the ESI.† The use of ΔV_{nr} and ΔIE_{PYSAs} has their advantages and disadvantages. The former is determined from the actual device, and hence, the value reflects the nature of the D:A interface; however, the value is not directly related to the energy offset. In contrast, the latter can be easily measured, although the value may be overestimated relative to the actual HOMO energy difference at the D:A interface owing to the contribution caused by charge-permanent multipole interactions, which are weakened at the interfacial mixed region. Because ΔV is a less direct measure of the energy offset than the others, it is not discussed hereinafter. Note that, as an alternative approach, temperature-dependent V_{OC} measurements allow us to estimate E_{CT} at 0 K by linear extrapolation.^{19,38,40,41} However, E_{CT} at room temperature is typically 0.1–0.2 eV higher than that at 0 K.^{40,41} Because we discuss the effect of slight energy offset differences, the uncertainty of 0.1–0.2 eV is undesirable; hence, the temperature-dependent V_{OC} measurements were not applied in this study.

Charge separation efficiency

We next measured the PL quenching yield Φ_q of the D:A blends after selective excitation of acceptors (Fig. S13–S15, ESI†). Fig. 3b shows the Φ_q s plotted against ΔV_{nr} . The Φ_q was close to unity when the energy offset was satisfactory (as a rule of thumb, in the region where ΔV_{nr} is larger than 0.2 V). Because the Φ_q is a product of the efficiencies of exciton harvesting at the D:A interfaces and charge transfer at the interface, the near-unity Φ_q indicates that all the excitons generated in the acceptor domains can reach the interface and quantitatively dissociate into the CT states. We have previously observed Y6 singlet exciton dynamics in PBDB-T-2F:Y6 blends using transient absorption (TA) spectroscopy.¹⁵ Upon selective photoexcitation of Y6, singlet excitons were generated in Y6 domains, which subsequently reached the D:A interface with a time constant of ~ 6 ps. Although the discussion on the intrinsic lifetime of Y6 singlet excitons is controversial,^{8,42} it is expected to be at least 200 ps, which is sufficient for all the excitons to reach the interface. Strikingly, the hole transfer from Y6 to PBDB-T-2F occurs with a sub-picosecond time scale despite the small energy offset of only 0.12 eV, resulting in the quantitative conversion of excitons to the CT states. In contrast, the quenching yield decreased in the region where ΔV_{nr} was less than 0.2 V. Because the exciton harvesting efficiency is independent of the energy offset,^{8,43} this result indicates that the



hole transfer rate decreases with a decrease in the energy offset, as is expected by Marcus theory in the normal region,^{14,16} leading to inefficient CT state formation.

To confirm this, we performed TA measurements for inefficient PBDB-T-2F-based blend films. The PBDB-T-2F:Y5 blend is a representative low-EQE_{PV} system (yellow triangles in Fig. 3) and suitable for comparison with the adequately investigated PBDB-T-2F:Y6 blend;^{15,44,45} thereby, the results for the PBDB-T-2F:Y5 blend are shown in the main text, whereas the results for other inefficient blends (Y1, Y2, and Y16) can be found in Fig. S16, ESI.† Since TA data for the inefficient blends are scarce (whereas there are quite a few for the efficient blends), these results will further deepen our understanding. Fig. 4a shows the TA spectra of the PBDB-T-2F:Y5 blend film after selective photoexcitation of Y5 at 800 nm. In analogy with the assignments for the PBDB-T-2F:Y6 system,^{15,42,44} the large photoinduced absorption (PIA) band observed at around 900 nm immediately after the photoexcitation can be attributable to Y5 singlet excitons, which gradually decayed thereafter. The broad negative signal observed in the 500–800 nm region is assigned to ground-state bleaching (GSB). In the case of the PBDB-T-2F:Y6 blend, the PBDB-T-2F GSB was observed in the 500–650 nm region already at 0 ps, evidencing the sub-picosecond hole transfer (Fig. S16a, ESI†). In contrast, close inspection of the GSB signal of the PBDB-T-2F:Y5 blend (Fig. 4b) revealed that the spectral shape in the 500–650 nm region at early times was different from that at later times, meaning that the GSB signal

in this region at 0 ps should mainly be ascribed to Y5 due to slow hole transfer. In addition, a rise in the PBDB-T-2F GSB signal was not observed in the PBDB-T-2F:Y5 blend, in sharp contrast to the PBDB-T-2F:Y6 blend, where the PBDB-T-2F GSB signal increased with a time constant of ~6 ps (Fig. S16a†).¹⁵ The rise in the PBDB-T-2F GSB signal was also not observed in other inefficient PBDB-T-2F-based blends (Fig. S16b–d†), indicating slower hole transfer in these inefficient blends than in the PBDB-T-2F:Y6 blend. Fig. 4c shows the time evolution of the TA signals monitored at 550 nm, where the TA signal was initially positive and then turned negative at later times, representing the decay of the Y5 excitons and the generation of the PBDB-T-2F GSB. The growth of the PBDB-T-2F GSB signal continued until at least 100 ps, again indicating slow hole transfer. Note that the later time TA kinetics at this wavelength includes the contribution of the geminate recombination of the CT states (*vide infra*); thereby, it is possible that the hole transfer occurred even after the appearance of the apparent peak at ~100 ps. These results confirmed that the slow hole transfer from Y5 (and also Y1, Y2, and Y16) to PBDB-T-2F was due to insufficient energy offsets.

To further deepen our understanding, EQE_{PV} was divided by Φ_q . Fig. 3c shows EQE_{PV}/ Φ_q plotted against ΔV_{nr} . Interestingly, EQE_{PV}/ Φ_q sharply decreased in the same region ($\Delta V_{nr} < 0.2$ V). EQE_{PV} can be expressed as:

$$EQE_{PV} = \eta_{abs} \times \eta_{ED} \times \eta_{CT} \times \eta_{CD} \times \eta_{CC} \quad (2)$$

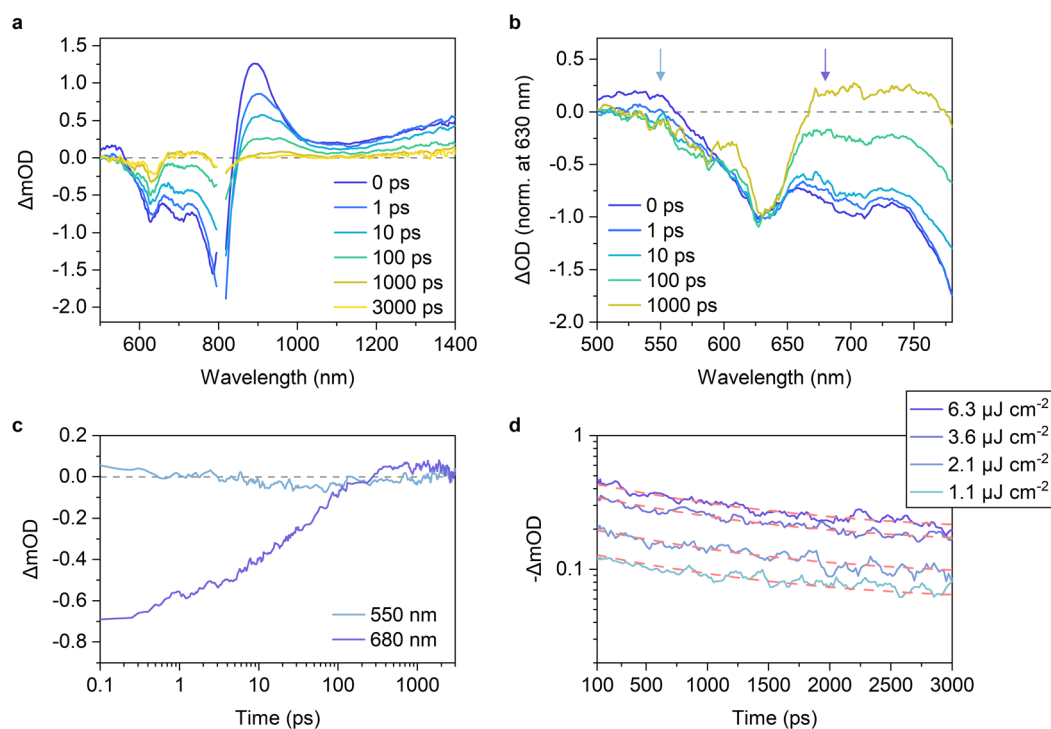


Fig. 4 (a) TA spectra of a PBDB-T-2F:Y5 blend film. The excitation wavelength was 800 nm with a fluence of $6.3 \mu\text{J cm}^{-2}$. (b) Normalized TA spectra of (a) at 630 nm (GSB peak of PBDB-T-2F). (c) Time evolution of the TA signals monitored at 550 and 680 nm. (d) Excitation-fluence dependence of the TA decays monitored at 630 nm. The red dashed lines represent the best fitting curves with the sum of an exponential function and a constant fraction, $\Delta mOD = a \exp(-t/\tau) + b$, where a , τ , and b are the fitting parameters and τ is shared for all the four decay curves. The charge dissociation efficiency was determined as $b/(a + b)$.



where η_{abs} , η_{ED} , η_{CT} , η_{CD} , and η_{CC} are the QYs of photon absorption, exciton diffusion to the D:A interface, charge transfer to form a CT state, long-range spatial dissociation of the CT state, and charge collection at the respective electrodes, respectively.^{8,9} Therefore, Fig. 3c represents the dependence of the long-range charge dissociation efficiency η_{CD} on the energy offset because $\Phi_{\text{q}} = \eta_{\text{ED}} \times \eta_{\text{CT}}$. Note that this assumes that η_{abs} and η_{CC} are independent of the energy offset. The former is evident. The latter is reasonable at least under short-circuit condition with a weak light illumination, such as in the EQE_{PV} measurements, because bimolecular charge recombination is suppressed under this condition.^{46,47} This assumption is verified by the good consistency between the measured J_{SC} (under 1 sun condition) and calculated J_{SC} obtained by integrating the EQE_{PV} (measured under short-circuit condition with a weak illumination) (Tables S4–S6, ESI†). Therefore, a decrease in EQE_{PV}/ Φ_{q} in the $\Delta V_{\text{nr}} < 0.2$ V region suggests that the long-range charge dissociation becomes inefficient when the energy offset is too small.

To confirm this, we measured the excitation-fluence dependence of the TA decays. Fig. 4d shows the recoveries of the PBDB-T-2F GSB under various excitation fluences. The decay kinetics were almost independent of the excitation fluence, indicating that the geminate recombination of the CT states was dominant under these excitation fluences.^{48–51} This is in sharp contrast to what we previously observed for the PBDB-T-2F:Y6 blend, where the geminate recombination was negligible and bimolecular recombination was significant even at low excitation fluences.¹⁵ Fig. 4c also shows the time evolution of the TA signals monitored at 680 nm. The negative signal, which is assigned to the Y5 GSB, slowly recovered and finally turned positive after 300 ps. This behavior was also observed for the other PBDB-T-2F-based blends, whereas the signal amplitude and the time at which the TA signal turned positive depended on the acceptors (Fig. S16, ESI†). We found that the positive signals at 680 nm of the inefficient blends were significantly small compared with that of the PBDB-T-2F:Y6 blend (Fig. 4c and S16, ESI†). In the PBDB-T-2F:Y6 blend, the TA signal turned positive already at 10 ps after photoexcitation and increased further. The positive signal at this wavelength is assigned to the transient electroabsorption (EA) signal of PBDB-T-2F.^{15,44,45,52} When an exciton dissociates into an electron–hole pair (CT state) at the D:A interface, the electron–hole pair generates a local electric field in the surroundings. This causes a Stark shift in the steady-state absorption of surrounding molecules, leading to the addition of a transient EA signal to the TA spectra.^{53,54} Because the transient EA signal increases with an increase in the separation distance of the electron–hole pair, our findings for the inefficient blends indicate that the charge dissociation in these blends is slow and inefficient. Therefore, the decay kinetics were fitted using an exponential function to determine the charge dissociation efficiency. The TA decay kinetics of the PBDB-T-2F:Y5 blend monitored at 630 nm (PBDB-T-2F GSB) were well fitted with the exponential function with a CT state lifetime of ~ 1.3 ns and the charge dissociation efficiency of only $\sim 42\%$ (Fig. 4d). Note that the charge dissociation efficiency obtained herein was lower than EQE_{PV}/ Φ_{q} of the

same blend ($\sim 46\%$) because TA measurements were performed under open-circuit condition, as will be discussed later.

We then measured the TA spectra of a PBDB-T:Y5 blend film to elucidate whether the low charge dissociation efficiency of the PBDB-T-2F:Y5 blend stems from the intrinsic nature of Y5 itself. The PBDB-T:Y5 blend exhibits a ΔV_{nr} of 0.234 V, which is above the threshold, and hence, comparison between the large-offset PBDB-T:Y5 and small-offset PBDB-T-2F:Y5 blends allows us to elucidate the origin of the inefficient charge dissociation in the PBDB-T-2F:Y5 blend. Fig. 5a shows the TA spectra of the PBDB-T:Y5 blend film in the visible region, where the assignments of the TA signals are the same as those of the above-mentioned PBDB-T-2F-based blends. We found that the hole transfer occurred in a sub-picosecond time scale in the PBDB-T:Y5 blend owing to the sufficient energy offset. Strikingly, the PBDB-T:Y5 blend exhibited considerably larger transient EA signals compared with the PBDB-T-2F:Y5 blend (Fig. 5b). In addition, the decay kinetics of the PBDB-T GSB depended on the excitation-fluence due to the contribution of the bimolecular recombination (Fig. S17, ESI†), which is indicative of efficient free carrier generation. These results are consistent with the relatively high J_{SC} of the PBDB-T:Y5 device. Therefore, we conclude that the low charge dissociation efficiency of the PBDB-T-2F:Y5 blend does not stem from the intrinsic nature of Y5 itself, but rather stems from the absence of sufficient energy offset at the D:A interface.

Our finding that the long-range spatial dissociation of CT states is inefficient when the energy offset is too small is very interesting. A key driver for the efficient charge dissociation in the representative efficient PBDB-T-2F:Y6 blend is attributed to the formation of a cascaded energy landscape near the D:A interface,¹⁵ which enables charges moving away from the interface without experiencing activation barriers because the attracting Coulomb barrier is compensated by the cascaded energy landscape. A possible explanation for the origin of the formation of the cascaded energy landscape relies on the large quadrupole moments of NFAs.^{34,37} Owing to a concentration gradient of NFAs near the D:A interface, charge–quadrupole interaction continuously increases with an increase in the distance from the interface, leading to the formation of a cascaded energy landscape (also referred to as band bending). Previous studies claimed that the drawback of the band bending was attributed to hole transfer becoming inefficient when the energy offset is too small.³⁴ In contrast, within the model proposed in ref. 34, once the CT states are formed through hole transfer, they are expected to efficiently dissociate into free carriers because the band bending is beneficial for charge dissociation. However, this study reveals that the decrease in the charge dissociation efficiency was more significant than the decrease in the hole transfer efficiency when the energy offset is too small (Fig. 3).

This is because decreasing the hole transfer rate does not necessarily result in low hole transfer efficiency as the hole transfer efficiency is determined by the competition with the intrinsic exciton decay rate. The hole transfer rate in the PBDB-T-2F:Y6 blend is more than 10^{12} s⁻¹, despite the small energy offset of 0.12 eV, as mentioned above. Therefore, even if we



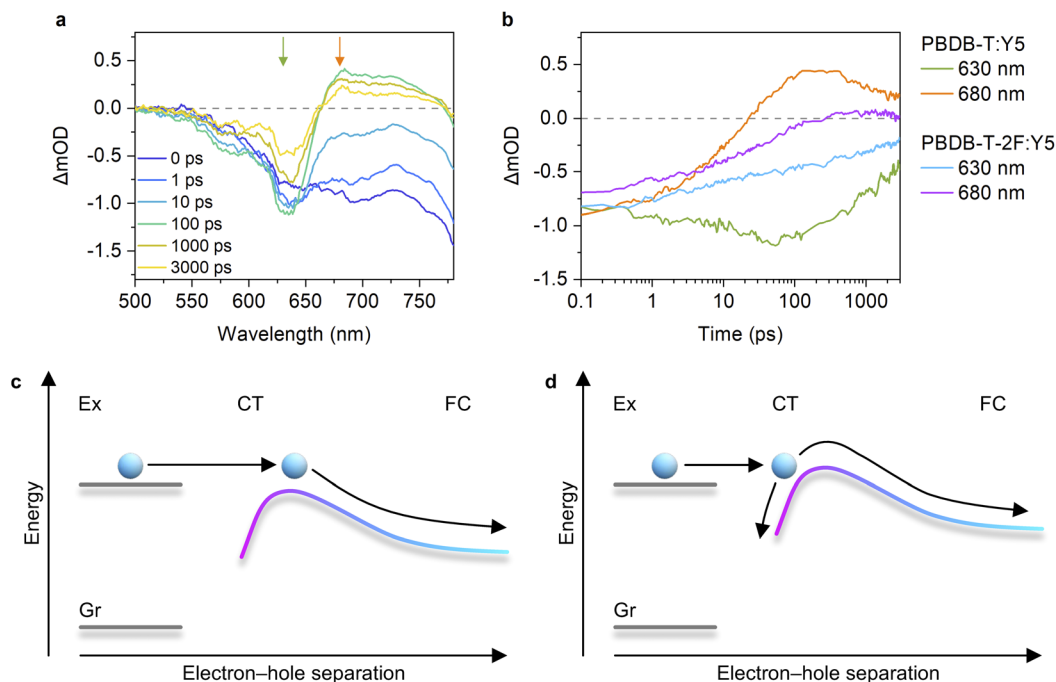


Fig. 5 (a) TA spectra of a PBDB-T:Y5 blend film. The excitation wavelength was 800 nm with a fluence of $6.2 \mu\text{J cm}^{-2}$. (b) Time evolutions of the TA signals of the PBDB-T:Y5 and PBDB-T-2F:Y5 blend films monitored at 630 nm (GSB peak of donor polymers) and 680 nm (transient EA). The excitation wavelength was 800 nm with fluences of $6.2 \mu\text{J cm}^{-2}$ (PBDB-T:Y5) and $6.3 \mu\text{J cm}^{-2}$ (PBDB-T-2F:Y5). Schematic showing the charge separation process in (c) efficient D:A blends and (d) inefficient D:A blends. Ex, CT, FC, and Gr refer to the excited state, CT state, free carrier, and ground state, respectively. (c) When the energy offset is sufficient, the initial separation distance between the electron and hole after isoenergetic charge transfer is satisfactory to overcome the activation barrier, resulting in barrier-less charge dissociation. (d) In contrast, when the energy offset is insufficient, charges need to overcome the activation barrier, resulting in poor charge dissociation efficiency.

assume that the hole transfer rate becomes an order of magnitude lower than that in the PBDB-T-2F:Y6 blend, the hole transfer rate remains on the order of 10^{11} s^{-1} , which is still larger than the intrinsic decay rate of acceptor excitons ($<5 \times 10^9 \text{ s}^{-1}$), leading to maintaining a relatively high hole transfer efficiency. In contrast, if the hole transfer becomes two orders of magnitude slower than that in the PBDB-T-2F:Y6 blend, the hole transfer efficiency should be significantly decreased. We estimated to what extent the hole transfer rate is decreased in the inefficient blends compared with the PBDB-T-2F:Y6 blend and found that the hole transfer rate supposedly remains only an order of magnitude lower (Fig. S18, ESI†).^{8,55}

We found that the CT state lifetime in the representative inefficient PBDB-T-2F:Y5 blend ($\sim 1.3 \text{ ns}$) was considerably shorter than that in the representative efficient PBDB-T-2F:Y6 blend ($\sim 2.6 \text{ ns}$, determined by the time-resolved PL spectroscopy¹⁵). This result implies that the CT states generated in the inefficient blends are more localized and tightly bound at the D:A interface.⁵¹ Therefore, we propose that, as schematically shown in Fig. 5c and d, there exists an activation barrier for charge dissociation, and hence, the QY of the long-range spatial dissociation depends on the initial separation distance of the CT states, which is affected by the energy offset. When the energy offset is sufficient, the initial separation distance between electron and hole after isoenergetic charge transfer is satisfactory for charges to overcome the activation barrier,

resulting in barrier-less charge dissociation. In contrast, when the energy offset is insufficient, charges need to overcome the activation barrier, resulting in poor charge dissociation efficiency. This model is similar to those developed for fullerene-based OSCs,^{11,12,53,56} except that the origin of the cascaded energy landscape in this model is attributed to the large quadrupole moment of NFAs. Although no clear experimental evidence that supports our hypothesis is yet available at the moment, our findings encourage us to further investigate the charge separation mechanism in future studies.

Impact of voltage loss on fill factor

We move our attention to the impact of voltage loss on FF. In general, a large V_{OC} is expected to provide a high FF.^{9,57,58} Nevertheless, as shown in Fig. 6a, the FFs of our devices decreased in the high V_{OC} region. To deepen our understanding, FF was plotted against ΔV_{nr} (Fig. 6b, see also Fig. S19, ESI†), where FF dropped in the $\Delta V_{\text{nr}} < 0.2 \text{ V}$ region, similar to the case of EQE_{PV} . This phenomenon can be rationalized by the following reasons. As is discussed in the previous section, the efficiency of the long-range charge dissociation is insufficient when the energy offset is too small. The charge dissociation efficiency η_{CD} of the PBDB-T-2F:Y5 blend obtained by TA measurements was lower than $\text{EQE}_{\text{PV}}/\Phi_{\text{q}}$ ($= \eta_{\text{abs}} \times \eta_{\text{CD}} \times \eta_{\text{CC}}$), as mentioned above. This indicates that the charge dissociation efficiency exhibits bias dependence because TA measurements



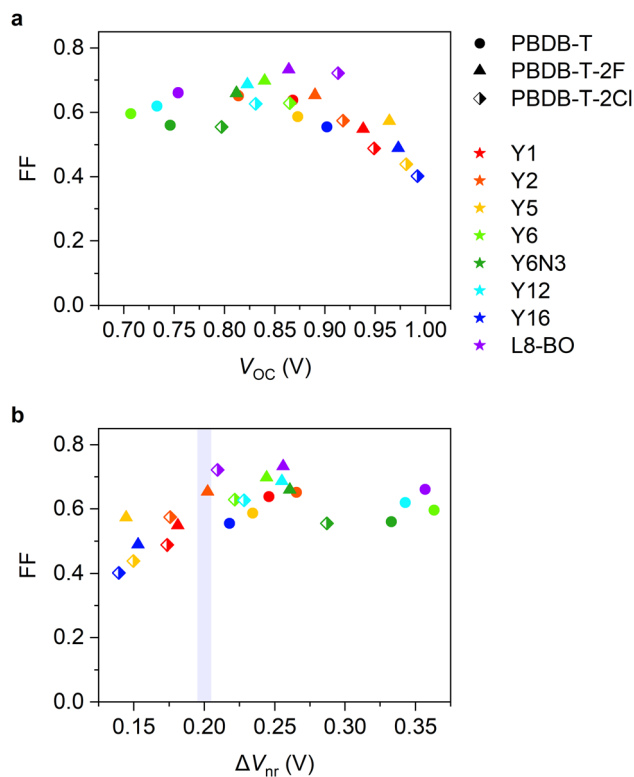


Fig. 6 FF plotted against (a) V_{OC} , and (b) ΔV_{nr} .

were performed under open-circuit condition, whereas EQE_{PV} was measured under short-circuit condition, where charge dissociation is accelerated with the aid of a large internal electric field.^{8,11,59,60} Therefore, the charge dissociation efficiency obtained by TA measurements being less than EQE_{PV}/Φ_q indicates that charge dissociation in inefficient devices becomes less efficient with an increase in the applied voltage in the forward direction, resulting in a poor FF.^{50,61} In addition, these devices may be more prone to suffer from bimolecular recombination loss. When a charge carrier encounters an opposite charge at the interface, a CT state is regenerated. If the CT state deactivates to the ground or lower-lying local triplet states, charge decay ultimately occurs. Instead, if the CT state redissociates into free carriers, bimolecular recombination is suppressed.^{46,47} With decreasing energy offset, the rate of radiative decay of the CT state and the rate of back charge transfer to the excited state are expected to increase, resulting in a less efficient redissociation of the CT state. Therefore, bimolecular recombination loss should be more severe for low-energy offset devices.

Our findings suggest that the trade-off between not only J_{SC} and V_{OC} , but also FF and V_{OC} should be managed. FFs of state-of-the-art OSCs have increased to ~ 0.8 , which significantly contributed to the improvement in the PCEs in the last two years.⁹ However, to the best of our knowledge, no OSCs with ΔV_{nr} far less than 0.2 V exhibited a FF of 0.8. This is probably due to the trade-off between FF and V_{OC} . Therefore, future research should focus more on overcoming the trade-off between FF and V_{OC} .

Ternary blend system

Finally, we demonstrated ternary blend OSCs consisting of two NFAs paired with a common donor to deepen our understanding on the interplay of the energy levels of the two NFAs. The two NFAs were selected based on the following criteria. The majority NFA was chosen such that a high EQE_{PV} and ΔV_{nr} being as close as possible to the threshold were achieved when paired with the common donor in the binary reference system. In contrast, the minority NFA was selected to achieve a low ΔV_{nr} of less than 0.18 V when paired with the common donor in the binary reference system. EQE_{PV} can be low in this case (all acceptors satisfying the criterion for ΔV_{nr} exhibit low EQE_{PV} s, as mentioned above). We stress that two NFAs in typical ternary OSCs are selected in a way such that reasonable device performances are obtained in binary references with the donor (and *vice versa*).^{1–6} In other words, two NFAs in typical ternary OSCs are selected such that both binary references exhibit ΔV_{nr} s of approximately or larger than 0.2 V and high EQE_{PV} s. In contrast, the minority NFA in this study was unique as it was chosen with only a small ΔV_{nr} , ignoring EQE_{PV} . In this way, the role of the two NFAs was emphasized, improving the clarity of future material design concepts.

The PBDB-T-2Cl:L8-BO device exhibited a high EQE_{PV} (maximum EQE_{PV} of 84.9% at 580 nm) with a moderate ΔV_{nr} of 0.209 V, which is approximately the threshold value that ensures a high EQE_{PV} (Fig. 3). In contrast, the PBDB-T-2Cl:Y1 device exhibited a low ΔV_{nr} of 0.174 V, whereas the EQE_{PV} was low (maximum EQE_{PV} was 36.1% at 580 nm). Therefore, we prepared ternary blend OSCs consisting of PBDB-T-2Cl, L8-BO, and Y1 as a common donor, majority NFA, and minority NFA, respectively, to understand the role of the two NFAs. Fig. 7a shows the EQE_{PV} spectra of the PBDB-T-2Cl:L8-BO:Y1 ternary blend devices with different blend ratios ($J-V$ characteristics and device parameters can be found in Fig. S20, S21 and Table S9, ESI[†]). The blend ratios were varied over 1:1.2- x : x , as indicated in the figure. Strikingly, EQE_{PV} remained almost unchanged even when x was varied from 0 to 0.3. EQE_{PV} was decreased when x was 0.4, although it was still considerably higher than that of the PBDB-T-2Cl:Y1 binary system ($x = 1.2$). The fact that the addition of a small amount of Y1 will not degrade the charge separation efficiency, despite the poor charge separation efficiency of the PBDB-T-2Cl:Y1 binary reference (Fig. 3 and S16, ESI[†]), suggests that charge separation preferentially occurs at the PBDB-T-2Cl:L8-BO interface, as schematically shown in Fig. 7d. When a Y1 exciton reaches the D:A interface, it will likely return to the bulk because the hole transfer is slow. On the other hand, the Y1 exciton can move to the L8-BO domain without a large energetic barrier because of similar excited state energies of L8-BO and Y1 (1.45 and 1.43 eV for L8-BO and Y1, respectively, Fig. S4, ESI[†]). Once the excitons are transferred to the L8-BO domains, they can quickly dissociate into the CT states. Therefore, charge separation preferentially occurs at the PBDB-T-2Cl:L8-BO interface, resulting in a high EQE_{PV} despite the addition of a small amount of Y1.

In contrast, V_{OC} continuously increased with an increase in the Y1 blend ratio. The detailed voltage loss analysis revealed



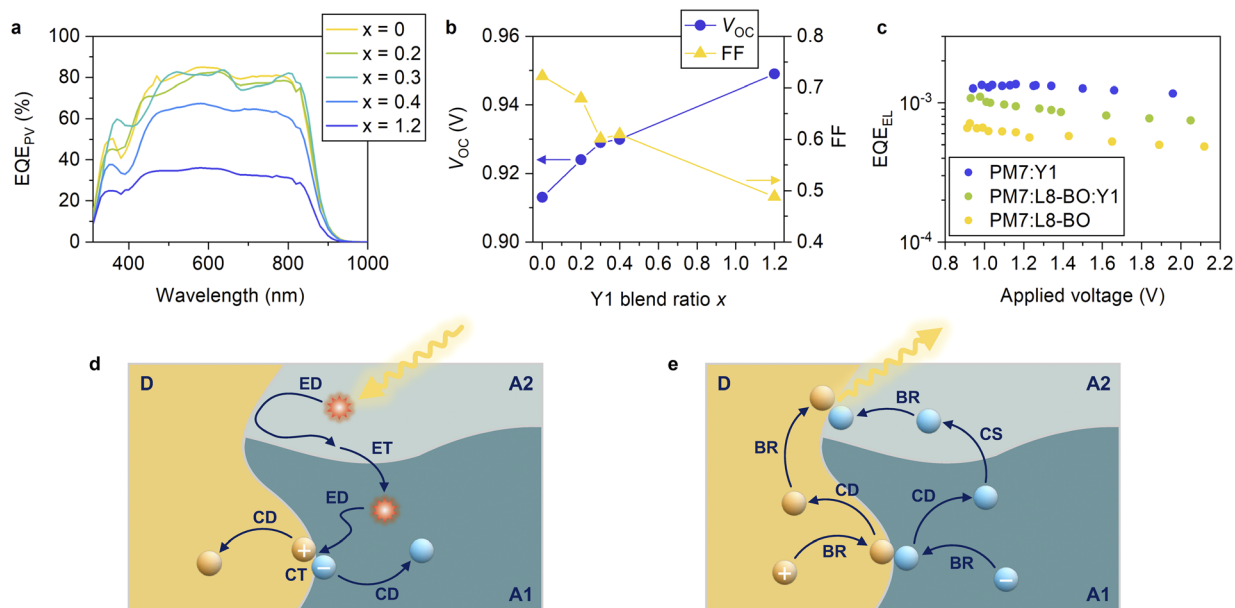


Fig. 7 (a) EQE_{PV} spectra of PBDB-T-2Cl:L8-BO:Y1 ternary blend devices with different blend ratios. The blend ratios were varied over 1 : 1.2- x : x , as indicated in the figure. (b) Blend ratio dependence of V_{OC} (blue circles, left axis) and FF (yellow triangles, right axis). (c) EQE_{EL} of the PBDB-T-2Cl:L8-BO:Y1 (1 : 1 : 0.2) ternary blend device as well as its binary references. (d) Schematic showing the charge separation process. Hole transfer is slow at the donor:minority NFA (D:A2) interface, and the CT states are not likely to form. On the other hand, excitons can move between the majority and minority NFA domains without a large energetic barrier. Therefore, charge separation preferentially occurs at the donor:majority NFA (D:A1) interface following exciton (energy) transfer from the minority to majority NFAs. ED, ET, CT, and CD refer to exciton diffusion, energy (exciton) transfer, charge transfer, and charge dissociation, respectively. (e) Schematic showing the charge recombination process. Because the redissociation of the CT state is less efficient at the D:A2 interface compared to that at the D:A1 interface, charge recombination is expected to be more likely to occur at the former. Because the EQE_{EL} of the D:A2 blend is higher than that of the D:A1 blend, the preferential recombination at the former leads to an increase in the EQE_{EL} of the ternary blend. BR and CS refer to bimolecular charge recombination to regenerate the CT states, and charge shift between A1 and A2, respectively.

that the ΔV_{nr} of the ternary blend device ($x = 0.2$) was 0.199 V, which was lower than that of the PBDB-T-2Cl:L8-BO binary reference (0.209 V) (Table S10, ESI[†]). To confirm this, we measured the external quantum efficiency of electroluminescence (EQE_{EL}) of an OSC device at forward biases because ΔV_{nr} is directly related to EQE_{EL} as follows:

$$\Delta V_{nr} = -\frac{k_B T}{q} \ln(EQE_{EL}) \quad (3)$$

where k_B and T are the Boltzmann constant and absolute temperature, respectively (EL spectra and ΔV_{nr} calculated using EQE_{EL} can be found in Fig. S22 and Table S10, ESI[†]).^{22-24,40,41} As shown in Fig. 7c, EQE_{EL} of the ternary blend device was apparently higher than that of the PBDB-T-2Cl:L8-BO binary reference. Rather, EQE_{EL} of the ternary blend device was close to that of the PBDB-T-2Cl:Y1 binary reference, especially at low applied voltages. The ΔV_{nr} s determined by the two methods were in accordance with each other within a small error (Table S10, ESI[†]), and ΔV_{nr} of the ternary blend device was smaller than that of the PBDB-T-2Cl:L8-BO binary reference in both methods. These results suggest that the PBDB-T-2Cl:Y1 interface preferentially served as a recombination center in the ternary blend, as schematically shown in Fig. 7e. Because the redissociation of the CT states is less efficient at the PBDB-T-2Cl:Y1 interface than that at the PBDB-T-2Cl:L8-BO interface, it is expected that charge recombination is more likely to occur

at the former. Because the EQE_{EL} of the PBDB-T-2Cl:Y1 blend is higher than that of the PBDB-T-2Cl:L8-BO blend, the preferential recombination at the PBDB-T-2Cl:Y1 interface leads to an increase in the EQE_{EL} of the ternary blend compared with that of the PBDB-T-2Cl:L8-BO blend. Therefore, the ternary blend OSCs consisting of a common donor paired with two NFAs, one with a high EQE_{PV} and the other with a low ΔV_{nr} , is expected to be an effective approach to overcome the trade-off between J_{SC} and V_{OC} . A remaining challenge with our ternary blend concept is that the trade-off between FF and V_{OC} has not been overcome. As shown in Fig. 7b, although an increase in the blend ratio of Y1 resulted in an increase in V_{OC} , it simultaneously decreased the FF. Therefore, both binary and ternary systems face the same challenge of overcoming the trade-off between FF and V_{OC} .

Conclusions

We have investigated the threshold to what extent the energy offset can be minimized for Y-series NFA-based OSCs. We found that the Y-series OSCs exhibited a clear threshold ΔV_{nr} of 0.2 V, below which EQE_{PV} sharply decreased. This is the reason why the ΔV_{nr} s of state-of-the-art OSCs remains approximately 0.2 V and very few studies have reported that ΔV_{nr} can be exceeded beyond the 0.2 V threshold while maintaining a high EQE_{PV} . It is easily expected from Marcus theory that the hole transfer rate



from the NFA to donor decreases with a decrease in the energy offset. In contrast, what is surprising in our findings is that the quantum efficiency of the long-range spatial dissociation of the CT states also decreased with a decrease in the energy offset. This behavior cannot be rationalized only by the recently proposed model wherein charge dissociation occurs *via* the downhill relaxation of charges through the cascaded energy landscape. We propose that there still exists an activation barrier for charge dissociation even when a NFA with a large quadrupole moment is used and the quantum efficiency of the long-range spatial dissociation depends on the initial separation distance of the CT states. If the initial separation distance between the electron and hole after isoenergetic charge transfer is satisfactory, barrier-less charge dissociation can be achieved; otherwise, charges need to overcome the activation barrier, resulting in poor charge dissociation efficiency. Another interesting finding of this study is the observation of a clear trade-off between FF and V_{OC} caused by the deterioration of the charge dissociation efficiency when the energy offset is too small. This may be another reason why the ΔV_{nr} s of state-of-the-art OSCs remained at approximately 0.2 V.

Although we have focused on PBDB-T:Y-series blends to minimize the difference in the chemical structure and associated changes in physical properties, the observed trends can be considered as general for other NFA systems.³⁴ As the threshold energy that can ensure high charge photogeneration quantum efficiencies may depend on the chemical structure,^{13,34,38} more efforts should be dedicated to unveiling the complete details of the charge separation mechanism. Extending a similar study to other donor:acceptor systems can reveal what determines the threshold energy and how the threshold energy can be reduced. In this way, clear material design guidelines can be obtained for further improving the PCE.

The role of the two NFAs in ternary blend OSCs was also elucidated. In this study, the majority NFA was selected such that a high EQE_{PV} and ΔV_{nr} being as close as possible to the threshold were achieved, whereas the minority NFA was chosen such that a low ΔV_{nr} of less than 0.18 V was achieved, ignoring EQE_{PV}. In this way, the role of the two NFAs was emphasized. We found that by introducing the minority NFA, V_{OC} could be increased while maintaining a high EQE_{PV}. This is likely because charge separation preferentially occurs at the donor-majority NFA interface, whereas charge recombination is more likely to occur at the donor-minority NFA interface. One drawback of this ternary blend concept is the decrease in FF upon the introduction of the minority NFA because of the same reason as that for the decrease in FF in binary blends with a too small energy offset. Therefore, future research should focus more on overcoming the trade-off between FF and V_{OC} . If this challenge can be overcome, the PCE of our ternary blend device can be further improved.

Author contributions

Y. T. conceived and directed the project. R. S., T. S. and K. K. fabricated the devices and measured their performances. R. S., S. N. and K. K. performed steady-state optical measurements. Y.

T. performed time-resolved optical measurements. R. S., T. S. and Y. T. analysed the data. Y. T. wrote the original version of the manuscript and all authors contributed to revising the manuscript. All authors have given approval to the final version of the manuscript.

Conflicts of interest

There are no conflicts to declare.

Acknowledgements

This study was partly supported by the JSPS KAKENHI grant numbers 21H02012, 21H05394, 22K19065, and 23H03951, JST PRESTO program grant number JPMJPR1874, and Ogasawara Toshiaki Memorial Foundation.

References

- 1 P. Bi, S. Zhang, Z. Chen, Y. Xu, Y. Cui, T. Zhang, J. Ren, J. Qin, L. Hong, X. Hao and J. Hou, *Joule*, 2021, 5, 2408–2419.
- 2 W. Gao, F. Qi, Z. Peng, F. R. Lin, K. Jiang, C. Zhong, W. Kaminsky, Z. Guan, C.-S. Lee, T. J. Marks, H. Ade and A. K.-Y. Jen, *Adv. Mater.*, 2022, 34, 2202089.
- 3 L. Zhu, M. Zhang, J. Xu, C. Li, J. Yan, G. Zhou, W. Zhong, T. Hao, J. Song, X. Xue, Z. Zhou, R. Zeng, H. Zhu, C.-C. Chen, R. C. I. MacKenzie, Y. Zou, J. Nelson, Y. Zhang, Y. Sun and F. Liu, *Nat. Mater.*, 2022, 21, 656–663.
- 4 C. He, Y. Pan, Y. Ouyang, Q. Shen, Y. Gao, K. Yan, J. Fang, Y. Chen, C.-Q. Ma, J. Min, C. Zhang, L. Zuo and H. Chen, *Energy Environ. Sci.*, 2022, 15, 2537–2544.
- 5 R. Sun, Y. Wu, X. Yang, Y. Gao, Z. Chen, K. Li, J. Qiao, T. Wang, J. Guo, C. Liu, X. Hao, H. Zhu and J. Min, *Adv. Mater.*, 2022, 34, 2110147.
- 6 L. Zhan, S. Li, Y. Li, R. Sun, J. Min, Z. Bi, W. Ma, Z. Chen, G. Zhou, H. Zhu, M. Shi, L. Zuo and H. Chen, *Joule*, 2022, 6, 662–675.
- 7 Y. Wei, Z. Chen, G. Lu, N. Yu, C. Li, J. Gao, X. Gu, X. Hao, G. Lu, Z. Tang, J. Zhang, Z. Wei, X. Zhang and H. Huang, *Adv. Mater.*, 2022, 34, 2204718.
- 8 Y. Tamai, *Aggregate*, 2022, 3, e280.
- 9 Y. Tamai, *Adv. Energy Sustainability Res.*, 2023, 4, 2200149.
- 10 M. A. Green and A. W. Y. Ho-Baillie, *ACS Energy Lett.*, 2019, 4, 1639–1644.
- 11 T. M. Clarke and J. R. Durrant, *Chem. Rev.*, 2010, 110, 6736–6767.
- 12 F. Gao and O. Inganäs, *Phys. Chem. Chem. Phys.*, 2014, 16, 20291–20304.
- 13 W. W. Li, K. H. Hendriks, A. Furlan, M. M. Wienk and R. A. J. Janssen, *J. Am. Chem. Soc.*, 2015, 137, 2231–2234.
- 14 H. Imahori, Y. Kobori and H. Kaji, *Acc. Mater. Res.*, 2021, 2, 501–514.
- 15 S.-i. Natsuda, T. Saito, R. Shirouchi, Y. Sakamoto, T. Takeyama, Y. Tamai and H. Ohkita, *Energy Environ. Sci.*, 2022, 15, 1545–1555.
- 16 R. A. Marcus, *Rev. Mod. Phys.*, 1993, 65, 599–610.



- 17 T. Saito, S.-i. Natsuda, K. Imakita, Y. Tamai and H. Ohkita, *Sol. RRL*, 2020, **4**, 2000255.
- 18 T. F. Hinrichsen, C. C. S. Chan, C. Ma, D. Palecek, A. Gillett, S. Chen, X. Zou, G. Zhang, H. L. Yip, K. S. Wong, R. H. Friend, H. Yan, A. Rao and P. C. Y. Chow, *Nat. Commun.*, 2020, **11**, 5617.
- 19 A. Karki, J. Vollbrecht, A. J. Gillett, P. Selter, J. Lee, Z. Peng, N. Schopp, A. L. Dixon, M. Schrock, V. Nádaždy, F. Schauer, H. Ade, B. F. Chmelka, G. C. Bazan, R. H. Friend and T.-Q. Nguyen, *Adv. Energy Mater.*, 2020, **10**, 2001203.
- 20 T. Saito, S.-i. Natsuda, R. Shirouchi, K. Imakita, K. Kohzuki and Y. Tamai, *Phys. Status Solidi A*, 2023, DOI: [10.1002/pssa.202300121](https://doi.org/10.1002/pssa.202300121).
- 21 W. Shockley and H. J. Queisser, *J. Appl. Phys.*, 1961, **32**, 510–519.
- 22 U. Rau, *Phys. Rev. B: Condens. Matter Mater. Phys.*, 2007, **76**, 085303.
- 23 J. Yao, T. Kirchartz, M. S. Vezie, M. A. Faist, W. Gong, Z. He, H. Wu, J. Troughton, T. Watson, D. Bryant and J. Nelson, *Phys. Rev. Appl.*, 2015, **4**, 014020.
- 24 U. Rau, B. Blank, T. C. M. Müller and T. Kirchartz, *Phys. Rev. Appl.*, 2017, **7**, 044016.
- 25 J. Benduhn, K. Tvingstedt, F. Piersimoni, S. Ullbrich, Y. Fan, M. Tropicano, K. A. McGarry, O. Zeika, M. K. Riede, C. J. Douglas, S. Barlow, S. R. Marder, D. Neher, D. Spoltore and K. Vandewal, *Nat. Energy*, 2017, **2**, 17053.
- 26 M. Azzouzi, J. Yan, T. Kirchartz, K. Liu, J. Wang, H. Wu and J. Nelson, *Phys. Rev. X*, 2018, **8**, 031055.
- 27 F. D. Eisner, M. Azzouzi, Z. Fei, X. Hou, T. D. Anthopoulos, T. J. S. Dennis, M. Heeney and J. Nelson, *J. Am. Chem. Soc.*, 2019, **141**, 6362–6374.
- 28 X.-K. Chen, D. Qian, Y. Wang, T. Kirchartz, W. Tress, H. Yao, J. Yuan, M. Hülsbeck, M. Zhang, Y. Zou, Y. Sun, Y. Li, J. Hou, O. Inganäs, V. Coropceanu, J.-L. Bredas and F. Gao, *Nat. Energy*, 2021, **6**, 799–806.
- 29 L. Zhu, J. Zhang, Y. Guo, C. Yang, Y. Yi and Z. Wei, *Angew. Chem., Int. Ed.*, 2021, **60**, 15348–15353.
- 30 M. B. Price, P. A. Hume, A. Ilina, I. Wagner, R. R. Tamming, K. E. Thorn, W. Jiao, A. Goldingay, P. J. Conaghan, G. Lakhwani, N. J. L. K. Davis, Y. Wang, P. Xue, H. Lu, K. Chen, X. Zhan and J. M. Hodgkiss, *Nat. Commun.*, 2022, **13**, 2827.
- 31 Z. Jia, Z. Chen, X. Chen, L. Bai, H. Zhu and Y. M. Yang, *J. Phys. Chem. Lett.*, 2021, **12**, 151–156.
- 32 F. Liu, L. Zhou, W. Liu, Z. Zhou, Q. Yue, W. Zheng, R. Sun, W. Liu, S. Xu, H. Fan, L. Feng, Y. Yi, W. Zhang and X. Zhu, *Adv. Mater.*, 2021, **33**, 2100830.
- 33 J. Zhang, W. Liu, G. Zhou, Y. Yi, S. Xu, F. Liu, H. Zhu and X. Zhu, *Adv. Energy Mater.*, 2020, **10**, 1903298.
- 34 S. Karuthedath, J. Gorenflot, Y. Firdaus, N. Chaturvedi, C. S. P. De Castro, G. T. Harrison, J. I. Khan, A. Markina, A. H. Balawi, T. A. D. Peña, W. Liu, R.-Z. Liang, A. Sharma, S. H. K. Paleti, W. Zhang, Y. Lin, E. Alarousu, D. H. Anjum, P. M. Beaujuge, S. De Wolf, I. McCulloch, T. D. Anthopoulos, D. Baran, D. Andrienko and F. Laquai, *Nat. Mater.*, 2021, **20**, 378–384.
- 35 J. Yuan, Y. Q. Zhang, L. Y. Zhou, G. C. Zhang, H. L. Yip, T. K. Lau, X. H. Lu, C. Zhu, H. J. Peng, P. A. Johnson, M. Leclerc, Y. Cao, J. Ulanski, Y. F. Li and Y. P. Zou, *Joule*, 2019, **3**, 1140–1151.
- 36 J. Bertrandie, J. Han, C. S. P. De Castro, E. Yengel, J. Gorenflot, T. Anthopoulos, F. Laquai, A. Sharma and D. Baran, *Adv. Mater.*, 2022, **34**, 2202575.
- 37 L. Perdigón-Toro, H. Zhang, A. Markina, J. Yuan, S. M. Hosseini, C. M. Wolff, G. Zuo, M. Stolterfoht, Y. Zou, F. Gao, D. Andrienko, S. Shoaee and D. Neher, *Adv. Mater.*, 2020, **32**, 1906763.
- 38 K. Kawashima, Y. Tamai, H. Ohkita, I. Osaka and K. Takimiya, *Nat. Commun.*, 2015, **6**, 10085.
- 39 T. Umeyama, K. Igarashi, D. Sasada, Y. Tamai, K. Ishida, T. Koganezawa, S. Ohtani, K. Tanaka, H. Ohkita and H. Imahori, *Chem. Sci.*, 2020, **11**, 3250–3257.
- 40 K. Vandewal, K. Tvingstedt, A. Gadisa, O. Inganäs and J. V. Manca, *Phys. Rev. B: Condens. Matter Mater. Phys.*, 2010, **81**, 125204.
- 41 K. Vandewal, K. Tvingstedt, J. V. Manca and O. Inganäs, *IEEE J. Sel. Top. Quantum Electron.*, 2010, **16**, 1676–1684.
- 42 S.-i. Natsuda, Y. Sakamoto, T. Takeyama, R. Shirouchi, T. Saito, Y. Tamai and H. Ohkita, *J. Phys. Chem. C*, 2021, **125**, 20806–20813.
- 43 Y. Tamai, H. Ohkita, H. Bente and S. Ito, *J. Phys. Chem. Lett.*, 2015, **6**, 3417–3428.
- 44 A. Karki, J. Vollbrecht, A. J. Gillett, S. S. Xiao, Y. Yang, Z. Peng, N. Schopp, A. L. Dixon, S. Yoon, M. Schrock, H. Ade, G. N. M. Reddy, R. H. Friend and T.-Q. Nguyen, *Energy Environ. Sci.*, 2020, **13**, 3679–3692.
- 45 A. J. Gillett, A. Privitera, R. Dilmurat, A. Karki, D. Qian, A. Pershin, G. Londi, W. K. Myers, J. Lee, J. Yuan, S.-J. Ko, M. K. Riede, F. Gao, G. C. Bazan, A. Rao, T.-Q. Nguyen, D. Beljonne and R. H. Friend, *Nature*, 2021, **597**, 666–671.
- 46 G. Lakhwani, A. Rao and R. H. Friend, *Annu. Rev. Phys. Chem.*, 2014, **65**, 557–581.
- 47 T. Fukuhara, Y. Tamai and H. Ohkita, *Sustainable Energy Fuels*, 2020, **4**, 4321–4351.
- 48 Y. Tamai, K. Tsuda, H. Ohkita, H. Bente and S. Ito, *Phys. Chem. Chem. Phys.*, 2014, **16**, 20338–20346.
- 49 Y. Tamai, *Polym. J.*, 2020, **52**, 691–700.
- 50 Y. Sakamoto, S. Izawa, H. Ohkita, M. Hiramoto and Y. Tamai, *Commun. Mater.*, 2022, **3**, 76.
- 51 S.-i. Natsuda, T. Saito, R. Shirouchi, K. Imakita and Y. Tamai, *Polym. J.*, 2022, **54**, 1345–1353.
- 52 P. Wan, X. Chen, Q. Liu, S. Mahadevan, M. Guo, J. Qiu, X. Sun, S.-W. Tsang, M. Zhang, Y. Li and S. Chen, *J. Phys. Chem. Lett.*, 2021, **12**, 10595–10602.
- 53 S. Gélinas, A. Rao, A. Kumar, S. L. Smith, A. W. Chin, J. Clark, T. S. van der Poll, G. C. Bazan and R. H. Friend, *Science*, 2014, **343**, 512–516.
- 54 Y. Tamai, Y. Fan, V. O. Kim, K. Ziabrev, A. Rao, S. Barlow, S. R. Marder, R. H. Friend and S. M. Menke, *ACS Nano*, 2017, **11**, 12473–12481.
- 55 Y. Zhong, M. Causa, G. J. Moore, P. Krauspe, B. Xiao, F. Gunther, J. Kublitski, R. Shivhare, J. Benduhn, E. BarOr, S. Mukherjee, K. M. Yallum, J. Rehault, S. C. B. Mannsfeld,



- D. Neher, L. J. Richter, D. M. DeLongchamp, F. Ortmann, K. Vandewal, E. Zhou and N. Banerji, *Nat. Commun.*, 2020, **11**, 833.
- 56 A. A. Bakulin, A. Rao, V. G. Pavelyev, P. H. van Loosdrecht, M. S. Pshenichnikov, D. Niedzialek, J. Cornil, D. Beljonne and R. H. Friend, *Science*, 2012, **335**, 1340–1344.
- 57 M. A. Green, *Solid-State Electron.*, 1981, **24**, 788–789.
- 58 J. Hou, O. Inganäs, R. H. Friend and F. Gao, *Nat. Mater.*, 2018, **17**, 119–128.
- 59 L. Onsager, *Phys. Rev.*, 1938, **54**, 554–557.
- 60 C. L. Braun, *J. Chem. Phys.*, 1984, **80**, 4157–4161.
- 61 S. Izawa and M. Hiramoto, *Nat. Photonics*, 2021, **15**, 895–900.

